



Title	Electron energy-loss spectroscopic evaluation of depth-dependent swelling of He <sup>+</sup> ion-irradiated 4H-SiC correlated with defect type
Author(s)	Yang, Subing; Nakagawa, Yuki; Kondo, Minako; Shibayama, Tamaki
Citation	Journal of Applied Physics, 127(17), 175106 <a href="https://doi.org/10.1063/1.5143399">https://doi.org/10.1063/1.5143399</a>
Issue Date	2020-05-07
Doc URL	<a href="http://hdl.handle.net/2115/81123">http://hdl.handle.net/2115/81123</a>
Rights	This article may be downloaded for personal use only. Any other use requires prior permission of the author and AIP Publishing. This article appeared in Journal of Applied Physics 127, 175106 (2020) and may be found at <a href="https://aip.scitation.org/doi/10.1063/1.5143399">https://aip.scitation.org/doi/10.1063/1.5143399</a>
Type	article
File Information	Journal of Applied Physics 127, 175106.pdf



[Instructions for use](#)

# Electron energy-loss spectroscopic evaluation of depth-dependent swelling of He<sup>+</sup> ion-irradiated 4H-SiC correlated with defect type

Cite as: J. Appl. Phys. **127**, 175106 (2020); <https://doi.org/10.1063/1.5143399>

Submitted: 23 December 2019 . Accepted: 16 April 2020 . Published Online: 04 May 2020

Subing Yang, Yuki Nakagawa , Minako Kondo, and Tamaki Shibayama 



View Online



Export Citation



CrossMark

## ARTICLES YOU MAY BE INTERESTED IN

[Electrocaloric effects in monolayer germanium sulfide: A study by molecular dynamics simulations and thermodynamic analyses](#)

Journal of Applied Physics **127**, 175105 (2020); <https://doi.org/10.1063/1.5139007>

[In situ XPS spectroscopic study of thermal stability of W/Ni bilayer Ohmic contact to n-type 4H-SiC](#)

Journal of Applied Physics **127**, 174501 (2020); <https://doi.org/10.1063/5.0002560>

[Deep learning in heterogeneous materials: Targeting the thermo-mechanical response of unidirectional composites](#)

Journal of Applied Physics **127**, 175101 (2020); <https://doi.org/10.1063/5.0002917>

Lock-in Amplifiers  
up to 600 MHz



Watch



# Electron energy-loss spectroscopic evaluation of depth-dependent swelling of He<sup>+</sup> ion-irradiated 4H-SiC correlated with defect type

Cite as: J. Appl. Phys. 127, 175106 (2020); doi: 10.1063/1.5143399

Submitted: 23 December 2019 · Accepted: 16 April 2020 ·

Published Online: 4 May 2020



Subing Yang,<sup>1</sup> Yuki Nakagawa,<sup>2</sup>  Minako Kondo,<sup>2</sup> and Tamaki Shibayama<sup>2,a)</sup> 

## AFFILIATIONS

<sup>1</sup>Graduate School of Engineering, Hokkaido University, Sapporo, Hokkaido 060-8628, Japan

<sup>2</sup>Faculty of Engineering, Hokkaido University, Sapporo, Hokkaido 060-8628, Japan

<sup>a)</sup>Author to whom correspondence should be addressed: shiba@qe.eng.hokudai.ac.jp

## ABSTRACT

Various defects and amorphous transitions are the primary mechanism behind the accumulation of swelling in silicon carbide (SiC). In this study, selected-area He<sup>+</sup> ion irradiation was carried out on single-crystal 4H-SiC using fluences of  $1 \times 10^{15}$ ,  $5 \times 10^{16}$ , and  $1 \times 10^{17} \text{ cm}^{-2}$  at room temperature. The defect distribution in the samples with varying irradiation fluences was analyzed using transmission electron microscopy (TEM), while the local swelling of regions under varying damage conditions was estimated using electron energy-loss spectroscopy. The results provide the range of swelling in SiC possessing different primary defect types, such as point defects or tiny clusters, black spot defects, and amorphous SiC. A saturation swelling with a value of 2%–3% in the near-surface region, induced by point defects or tiny clusters (invisible in TEM), was observed at room temperature over the fluence range of  $1 \times 10^{15}$  to  $1 \times 10^{17} \text{ cm}^{-2}$ . This saturation has already reached at a great low dose of about 0.02 dpa. The swelling of the region containing black spot defects ranges from about 3% to 7%. Helium bubbles increase the volume swelling of SiC, while the He<sup>+</sup> ion irradiation may also perform a decreasing effect on the volume swelling below a certain irradiation fluence.

Published under license by AIP Publishing. <https://doi.org/10.1063/1.5143399>

## I. INTRODUCTION

Owing to its excellent mechanical and structural properties, silicon carbide (SiC) has been proposed for structure and cladding materials for a nuclear and an aerospace environment.<sup>1–3</sup> In these harsh environments, however, the high-dose irradiation will induce swelling and creep in SiC-based components, degrading the mechanical property of the SiC and greatly decreasing the lifetime of the SiC-based components.<sup>3</sup> Functionally, owing to its superior electronic, optical, and physical properties, SiC is also an important wide-bandgap semiconductor material with applications in high-temperature, high-power, and high-frequency electronic devices.<sup>4,5</sup> For fabrication of the SiC devices, ion implantation is used to selectively dope with certain carrier particles, controlling the concentration over a well-defined depth. However, ion implantation will also inevitably introduce great strain and swelling in the materials. This strain and swelling, measured by electron backscattering diffraction and Raman spectroscopy in our previous investigation,<sup>6</sup> has been found to significantly change the mechanical and electronic

properties of the SiC devices.<sup>5</sup> Thus, a fundamental understanding of the strain and swelling accumulation in irradiated SiC is important for such applications.

Up to now, considerable research efforts have been made to explore the swelling in SiC after neutron irradiation<sup>7–9</sup> and ion implantation.<sup>1,3,10</sup> It is generally accepted that defects introduced by irradiation play an important role in the strain and swelling accumulation. Under varying irradiation conditions, including varying temperatures<sup>2</sup> or irradiation fluences,<sup>11</sup> the swelling changes greatly because of different types of defects formed under different irradiation conditions, i.e., point defects, defect clusters, voids, and bubbles. For instance, at temperatures sufficiently high for vacancy mobility, swelling will result from vacancy accumulation in a void.<sup>12</sup> Below this critical temperature, however, the swelling mainly results from point defects (interstitial and vacancy) and/or point defect clusters.<sup>7</sup> Moreover, the swelling mechanism becomes more complex when low-mass particles, such as H<sup>+</sup> or He<sup>+</sup>, are produced or implanted into the materials owing to the

bubbles formed by the low-mass particles.<sup>11,13</sup> Therefore, it is critical to clarify the swelling induced by each defect type. However, the contribution to the swelling of each defect type in the irradiated SiC is understood but little.

In previous irradiation studies, and especially for ion irradiation, the swelling is typically measured via a dimensional change using x-ray diffraction<sup>8</sup> or atomic force microscopy,<sup>1</sup> where the swelling is usually the result of the summation of various defect types, including point defects, defect clusters, and even amorphous transitions. Using these characterization methods, however, it is difficult to separate the contribution to the swelling of each defect type. Bae *et al.* measured the local volume swelling in the Pt ion-irradiated 6H-SiC using electron energy-loss spectroscopy (EELS), which provided direct evidence of defect generation as a mechanism for initial volume swelling,<sup>14</sup> but they did not give a clear swelling range for different type defects or damages either. When considering that the swelling significantly changes under varying irradiation fluences and temperatures, basically owing to the variation of the primary defect type or microstructure, a better swelling predictor may be the development of a direct correlation between swelling and defect types. To determine the contribution to the swelling of different types of defects or damages, various defects/damages should be separately introduced into the SiC. It was reported that the critical amorphization temperature of SiC is about 400–650 K.<sup>15,16</sup> The ion irradiation at room temperature is supposed to introduce amorphization of SiC as well as some other defects and damages. In addition, this irradiation is also helpful to explore the ion irradiation effects on SiC at a relative low temperature, which would happen for some SiC applications such as in an aerospace environment. In addition, a local swelling detection method is also needed. The EELS shows a correlation between the low-loss spectrum and the material density and has a relatively high resolution performed under scanning transmission electron microscopy (STEM).<sup>17</sup> Therefore, EELS can be used to locally estimate the swelling of different damage regions.

This study uses He<sup>+</sup> ion irradiation at room temperature to introduce various damage levels and defect types as a function of depth into 4H-SiC. Various transmission electron microscopy (TEM) techniques were used to determine the defect distribution in the SiC, and the local swelling in different regions was separately evaluated by EELS. This study clarifies the contribution of different defect types to the volume swelling in SiC, which may be helpful for the prediction of SiC swelling in applications.

## II. EXPERIMENTAL PROCEDURES

### A. Irradiation experiment and microstructural characterization

Single-crystalline n-type 4H-SiC (0001) substrates of  $10 \times 10 \times 0.33 \text{ mm}^3$  in size (Xiamen Powerway Advanced Material Co., Ltd, Xiamen, China) were used herein. These substrates were irradiated with 100 keV He<sup>+</sup> ions at room temperature with varying fluences of  $1 \times 10^{15}$ ,  $5 \times 10^{16}$ , and  $1 \times 10^{17} \text{ cm}^{-2}$ . To perform the selected-area ion irradiation, part of the sample was covered with a mask during irradiation, and further details of the selected-area ion irradiation are given in Ref. 6. The penetration profile of He<sup>+</sup> ions into SiC was calculated by the SRIM 2013 software using a full

damage cascade model with the assumption of a sample density of  $3.21 \text{ g cm}^{-3}$ , while the threshold displacement energies for the C and Si sub-lattices used in the calculation were 21 and 35 eV,<sup>18</sup> respectively. The total penetration depth predicted by the calculation was about 600 nm with a maximum doping at about 450 nm.

After irradiation, cross-sectional thin foils for TEM characterization were fabricated from the irradiated areas with a focused ion-beam (FIB) system (JEOL, JEM-90320FIB) using gallium ions and an ion accelerating voltage of 30 kV. The microstructure of the irradiated 4H-SiC was observed by TEM (JEOL, JEM-2000FX) and high-resolution TEM (JEOL, JEM-2010F) at an operating voltage of 200 kV for both instruments. The EELS studies were carried out using Cs-corrected STEM (FEI, Titan G2 60-300) at an operating voltage of 300 kV. The EELS spectra were acquired via a high-angle annular dark-field STEM mode using the point-to-point detection method from different damaged regions with a beam size of about 0.2 nm, where three different positions at the same depth were acquired to obtain statistical results. To avoid the surface curvature and the possible damage introduced into the surface during the FIB processing, the EELS spectral acquisition began from a position about 50 nm beneath the surface. The peak location shifts of the EELS spectra were obtained after calibrating the zero-loss peak of each EELS spectrum. The energy resolution, measured as the full width at half maximum of the zero-loss peak, was 0.9 eV.

Finally, to detect irradiation damages in the samples, Raman backscattering was performed at room temperature using a Raman microscope (HORIBA XploRA), which used a 532 nm-wavelength laser, a 2400 groove/nm grating, and a  $100\text{--}1800 \text{ cm}^{-1}$  scanning range. The laser was focused to a spot  $\sim 2 \mu\text{m}$  in diameter, whereupon the Raman spectra were collected using the confocal Raman microscopy technique with a confocal aperture of  $100 \mu\text{m}$ .

### B. Swelling estimation methods using EELS

The plasmon-loss peak depends upon the density of the free electrons in the material. Specifically, when an electron beam generates a plasmon with the frequency  $\omega_p$ , the plasmon energy,  $E_p$ , is given by<sup>17</sup>

$$E_p = \frac{h}{2\pi} \omega_p = \frac{h}{2\pi} \left( \frac{ne^2}{\epsilon_0 m} \right)^{\frac{1}{2}}, \quad (1)$$

where  $E_p$  is the energy lost by the electron beam;  $h$  is Planck's constant;  $n$  is the free electron density;  $e$  and  $m$  are the electron charge and effective mass, respectively; and  $\epsilon_0$  is the permittivity of the free space.

According to the jellium model,  $n$  is proportional to the bulk density of the material.<sup>17</sup> Assuming that the observed decrease in the volume plasmon energy is solely attributed to the volume swelling of the specimen, the relation of volume swelling to the plasmon-loss peak shift can be given as<sup>19</sup>

$$\Delta V/V_0 = [V - V_0]/V_0 = [E_{p0}/E_p]^2 - 1, \quad (2)$$

where  $V_0$  and  $V$  are the material volumes before and after irradiation, respectively, and  $E_{p0}$  and  $E_p$  are the plasmon-loss peak positions of unirradiated and irradiated regions, respectively.

### III. RESULTS

#### A. Defect distribution in irradiated 4H-SiC

After irradiation with varying ion fluences, the internal microstructure of the He<sup>+</sup> ion-implanted 4H-SiC samples was observed by TEM along the [1120] orientation, as shown in Fig. 1. Combining these images with the irradiation dose (displacements per atom, dpa) and He<sup>+</sup> ion distribution profiles simulated by

SRIM 2013, three types of regions with distinct bright-field image contrasts (i.e., gray, black, and white) are discernible in the sample irradiated with a fluence of  $5 \times 10^{16} \text{ cm}^{-2}$  and are denoted as A-, B-, and C-layers in Fig. 1(a). The black-contrast B-layer region is further separated into two layers designated as the B<sub>1</sub>- and B<sub>2</sub>-layers. As derived from the TEM image contrast and the selected-area diffraction pattern (shown for each corresponding region) for the  $5 \times 10^{16} \text{ cm}^{-2}$  irradiation fluence, the near-surface

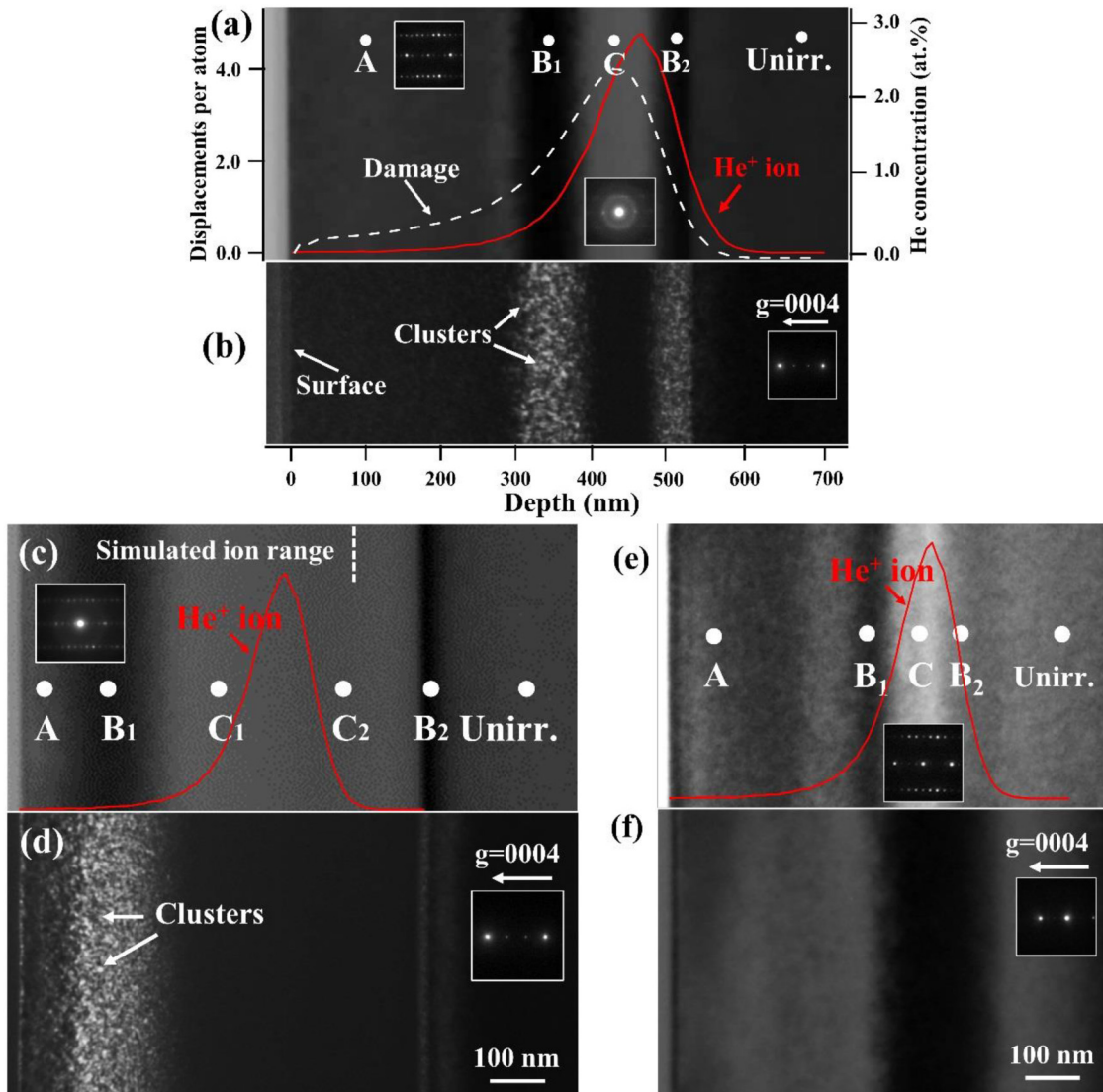


**FIG. 1.** Internal microstructure of 4H-SiC irradiated with He<sup>+</sup> ions with varying fluences. (a) and (b) Fluence of  $5 \times 10^{16} \text{ cm}^{-2}$ . (a) Cross-sectional image obtained along the [1120] zone including the depth distribution of the displacement damage (white dashed line) and the He<sup>+</sup> ion concentration (red solid line). (b) Weak-beam dark-field TEM image under the  $g/3g$ ,  $g=0004$  condition. (c) and (d) Fluence of  $1 \times 10^{17} \text{ cm}^{-2}$ . (c) Image obtained near the [1120] zone and (d) a weak-beam dark-field TEM image under the  $g/3g$ ,  $g=0004$  condition. (e) and (f) Fluence of  $1 \times 10^{15} \text{ cm}^{-2}$ . (e) Image obtained near the [1120] zone and (f) a two-beam bright-field TEM image under the  $g=0004$  condition. The inset images in (a), (c), and (e) are the selected-area diffraction pattern of the constituent areas, and the inset images in (b), (d), and (f) correspond to the diffraction condition when taking each image.

layer (i.e., the A-layer) contains only minimal damage and still maintains good crystallinity. However, the microstructure reaches an amorphous state at the maximum damage region (i.e., the C-layer) under this irradiation fluence, where the amorphous layer encompasses a depth range of 380–470 nm beneath the surface, with an amorphous layer thickness of 90 nm. In addition, the two black layers ( $B_1$ - and  $B_2$ - layers), adjacent to the amorphous region, contain significant defects as shown in the weak-beam dark-field image [Fig. 1(b)]. These defects are called black spot defects (BSDs)<sup>20</sup> and are a type of point defect clusters comprising interstitials and/or vacancies that occur in irradiated SiC, exhibiting a black contrast in bright-field TEM images and a white contrast in dark-field TEM images.

At a fluence of  $1 \times 10^{17} \text{ cm}^{-2}$ , greater damage was introduced into the material, resulting in an expansion of the amorphous layer from 250 nm beneath the surface to a depth of 700 nm, with an amorphous layer thickness of about 450 nm [Figs. 1(c) and 1(d)]. This damaged layer thickness is greater than that given by the SRIM simulation. This discrepancy between simulations and experiments may be mainly attributed to the decreasing density and the concurrent volume expansion during ion implantation, which is not considered in the SRIM calculation.<sup>21</sup> Furthermore, the near-surface region exhibits a gray contrast, and the bottom BSD region becomes very narrow in the samples irradiated with a fluence of  $1 \times 10^{17} \text{ cm}^{-2}$ . These different damage regions in this sample are also denoted as A-, B-, and C-layers based on their TEM image contrast. It should be noted that the C-layer region is further divided into  $C_1$ - and  $C_2$ -layers depending upon whether or not the layer contains helium bubbles, which will be shown and discussed later in the paper. For the sample irradiated with the smallest fluence of  $1 \times 10^{15} \text{ cm}^{-2}$ , the sample also exhibits different contrasts as a function of depth owing to varying levels of damages [Figs. 1(e) and 1(f)], but the contrast among different damage layers is relatively weaker than those observed in the above two samples [Figs. 1(a) and 1(c)] because of its lower irradiation fluence. In addition, no amorphous region or BSDs are observed under this fluence. However, a black contrast is seen at the maximum damage region in the two-beam bright-field TEM image [Fig. 1(e)], indicating some microstructure variations in this region. For convenient comparison of the above results, we also denote the damage regions in this sample as A-,  $B_1$ -,  $B_2$ -, and C-layers based on the TEM bright image contrast, despite different damage states between this and the other two irradiation fluence samples.

## B. Estimation of local swelling in different damage regions

The EELS low-loss spectra of different damage regions marked as the A-,  $B_1$ -,  $B_2$ -, C-,  $C_1$ -, and  $C_2$ -layers in Figs. 1(a), 1(c), and 1(e) were acquired and are shown in Figs. 2(a), 2(b), and 2(c), respectively. The volume plasmon-loss peak of the unirradiated region was located at 22.2 eV, which is consistent with previous results.<sup>19,22</sup> The volume plasmon-loss peak exhibits an apparent red shift in the damaged regions (A-, B-, and C-levels) for samples irradiated with fluences of  $5 \times 10^{16}$  and  $1 \times 10^{17} \text{ cm}^{-2}$ , where the shift increases with the increasing damage level. A red shift of the EELS plasmon-loss peak is also observed in the sample with the lowest fluence, as

shown in Fig. 2(c), but the magnitude of the shift is significantly smaller than the other two samples. In addition, the plasmon-loss peak shift of the C-level spectrum is smaller than that of the  $B_1$ -level spectrum in the low-fluence sample [Fig. 2(c)], where the former exhibited the largest peak shift in the samples with higher fluences, as shown in Figs. 2(a) and 2(b). This suggests that some variations in the microstructure may be introduced into the maximum damage region at this lowest ion irradiation fluence.

Based on the peak shift of the volume plasmon-loss EELS spectra, the local volume swelling in the different damage regions is estimated in Fig. 3. For better understanding, the estimated irradiation dose (dpa) profiles were also added into these figures. For the highest fluence, the simulated result of SRIM is deviated from the experimental one due to the expansion of the amorphous region [Fig. 1(c)]. However, the calculated dose of the first half damage region (about prior to 350 nm) should agree with the experimental result because this region still maintains some extent crystallinity. Therefore, only the first half of the dose (dpa) profile was added into Fig. 3(b). Owing to varying damages of each depth level, the defects for the ion-irradiated SiC vary as a function of depth, which also induces varying swelling as a function of depth. These estimated volume swelling results indicate a gradual increase of 1.9%–13.3% with increasing depth from the A- to C-layer, respectively, followed by a sharp decrease in the  $B_2$ -layer, which matches well with the shape of the dose profile [Fig. 3(a)]. The depth dependence of the swelling changes significantly for different irradiation fluences, both for the volume swelling trend and value, as shown in Figs. 3(b) and 3(c). The swelling in the sample irradiated with a  $1 \times 10^{17} \text{ cm}^{-2}$  fluence exhibits a sharp increase with increasing depth (i.e., from 3.2% to 15.3%), which should be attributed to the sharp increase of the irradiation dose [Fig. 3(b)]. The sample irradiated with a  $1 \times 10^{15} \text{ cm}^{-2}$  fluence, however, exhibited swelling that remained almost constant in the near-surface region and then gradually decreases in the C- and  $B_2$ -layers of the sample. The depth dependence of swelling under varying irradiation fluences will be discussed in terms of irradiation doses and microstructural variations in Secs. IV and V.

## IV. DISCUSSION

### A. Swelling saturation in the near-surface region

In the near-surface layer (i.e., the A-layer), no obvious defects are observed using TEM [Figs. 1(a) and 1(b)], though the volume of this layer expands by 1.9%–2.8%, as shown in Fig. 3(a). Using high-resolution TEM, the microstructure in the A-layer is observed to maintain a good crystallinity without obvious defects [Fig. 4(a)], while the defect contrast indicative of BSDs and amorphization is distinct around the  $B_1$ /C-layer interface. Hence, the volume swelling in the A-layer could be attributed to the formation of defects invisible to TEM, such as point defects or tiny defect clusters. For the sample irradiated with a fluence of  $1 \times 10^{15} \text{ cm}^{-2}$ , there is also no visible defect in TEM as shown in Fig. 1(f). However, using confocal Raman microscopy, a slight Si–Si vibration was observed in this sample as shown in Fig. 5, indicating the presence of Si interstitials. As the fluence increases to  $1 \times 10^{17} \text{ cm}^{-2}$ , the estimated swelling at the center of the A-layer is about 3.2%, which is similar to the maximum swelling of the A-layer in Fig. 3(a). In addition,

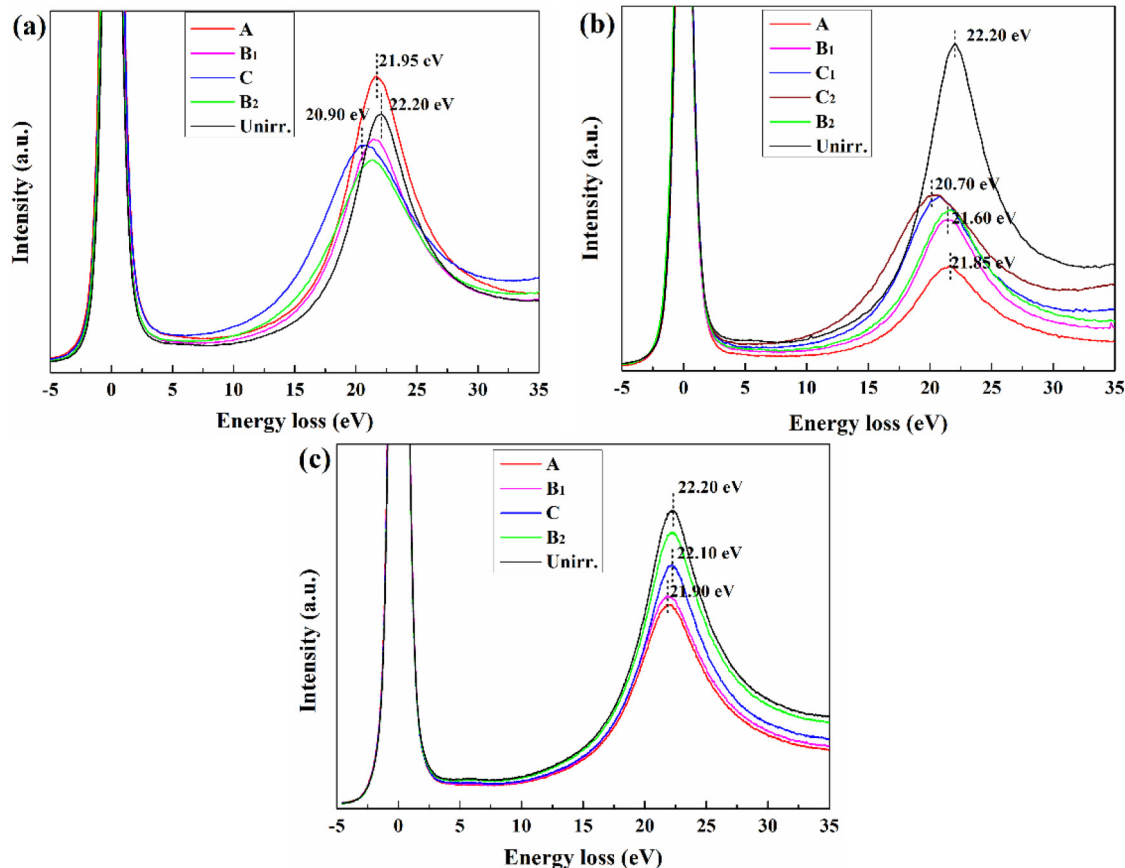


**FIG. 2.** Low-loss EELS spectra of different damage regions in samples irradiated with fluences of (a)  $5 \times 10^{16}$ , (b)  $1 \times 10^{17}$ , and (c)  $1 \times 10^{15} \text{ cm}^{-2}$ . The spectra in (a)–(c) correspond to the regions marked in Figs. 1(a), 1(c), and 1(e), respectively.

both critical doses of these two samples between A and B<sub>1</sub> layers are about 1.5 dpa. In the dark-field TEM image, a few small defect clusters can be observed in this A-layer [Fig. 1(d)], indicating that excess point defects begin to form visible clusters in the A-layer at this irradiation dose. This swelling value, therefore, may correspond to the maximum volume swelling induced by point defects or tiny clusters.

The  $1 \times 10^{15} \text{ cm}^{-2}$  fluence is quite low compared with the other two fluences. However, the swelling in the near-surface (i.e., A- and B<sub>1</sub>-layers) of the sample irradiated by this lowest fluence is almost the same as that of the near-surface (i.e., the A-layer) of samples irradiated by the other two fluences, which is around 2%–3%. Furthermore, no obvious defects are observed in the A- and B<sub>1</sub>-layers of this lowest-fluence sample in the bright-field TEM images [Figs. 1(e) and 1(f)]. The appearance of Si–Si vibrations in the Raman spectrum of this sample confirms the presence of Si interstitials as shown in Fig. 5. Therefore, similar swelling values of these near-surface regions indicate that a saturation of swelling is reached in this region, where only point defects or tiny clusters are supposed to be created. Moreover, as shown in Fig. 3(c), this

saturation of swelling has already reached at the beginning of irradiation with a dose of about 0.02 dpa. Besides, the width of this saturation swelling region gradually decreases with the increasing irradiation fluence owing to the expansion of the BSDs and/or amorphous layer.

## B. Swelling in the BSD-containing region

The BSDs are observed in the B<sub>1</sub>-layer of samples irradiated with fluences of  $5 \times 10^{16}$  and  $1 \times 10^{17} \text{ cm}^{-2}$ , where the average BSD size is 6.4 and 7.7 nm, respectively, at BSD number densities of  $2.6 \times 10^{22}$  and  $3.7 \times 10^{22} \text{ m}^{-3}$ , respectively. The swelling in the center of the B<sub>1</sub>-layer of the sample irradiated with the fluence of  $5 \times 10^{16}$  ( $1 \times 10^{17}$ )  $\text{cm}^{-2}$  is 4.9% (5.7%), where the slight increase in swelling of the latter sample may be attributed to its relatively larger BSD size and number density. Moreover, the swelling of the B<sub>1</sub>-layer in both of these samples ranges from about 3% to 7% with a dose range of about 1.5–3.4 dpa [Fig. 3(a) and 3(b)]. Katoh *et al.*<sup>10</sup> reported a maximum swelling of 3C–SiC prior to amorphization of about 7% under Ni<sup>3+</sup> irradiation at 333 K, which agrees

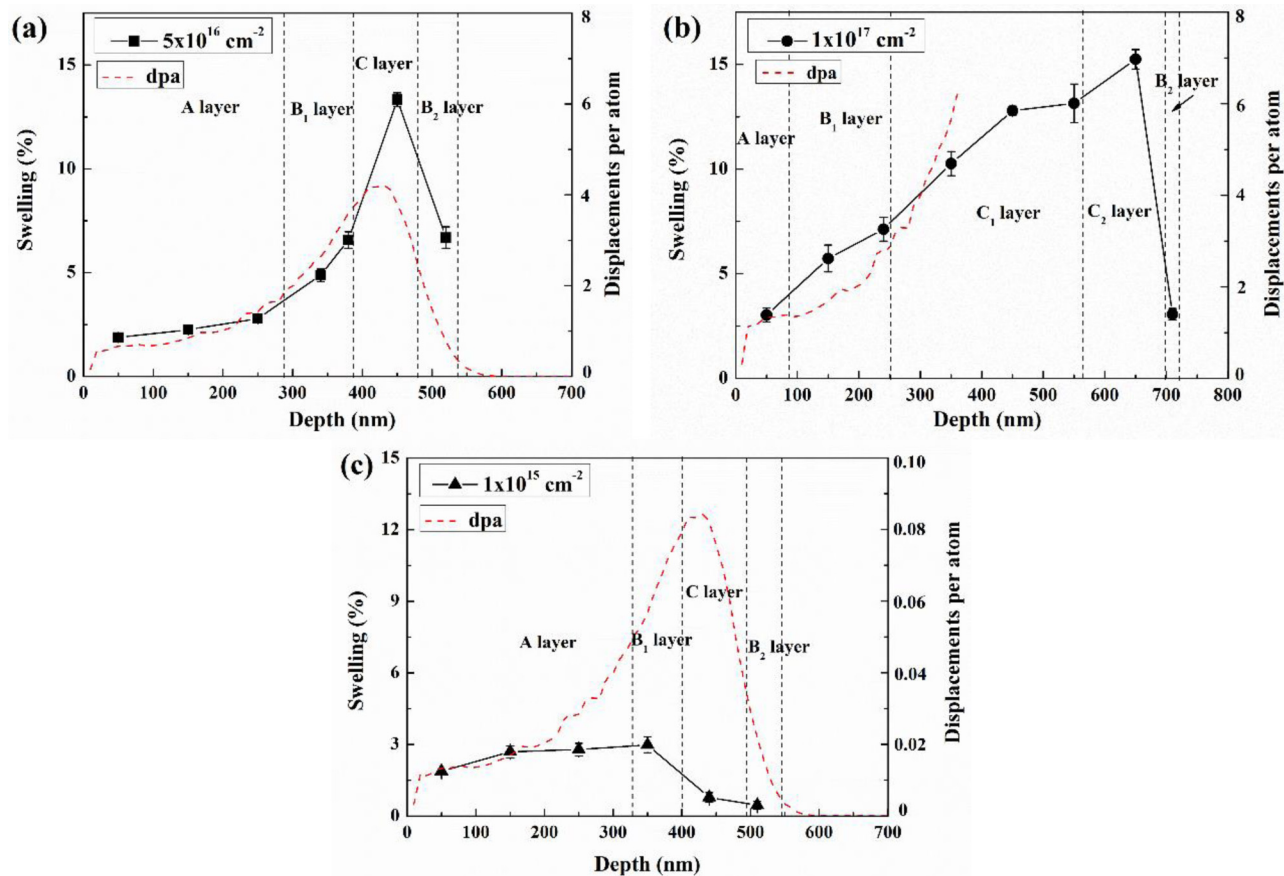


FIG. 3. Profile of swelling as a function of depth combined with the estimated dose profile in selected-area He<sup>+</sup> ion-irradiated 4H-SiC irradiated at fluences of (a)  $5 \times 10^{16}$ , (b)  $1 \times 10^{17}$ , and (c)  $1 \times 10^{15}$  cm<sup>-2</sup>. Only the first half of the dose (dpa) profile was added into Fig. 3(b) due to the expansion of the amorphous region at this fluence.

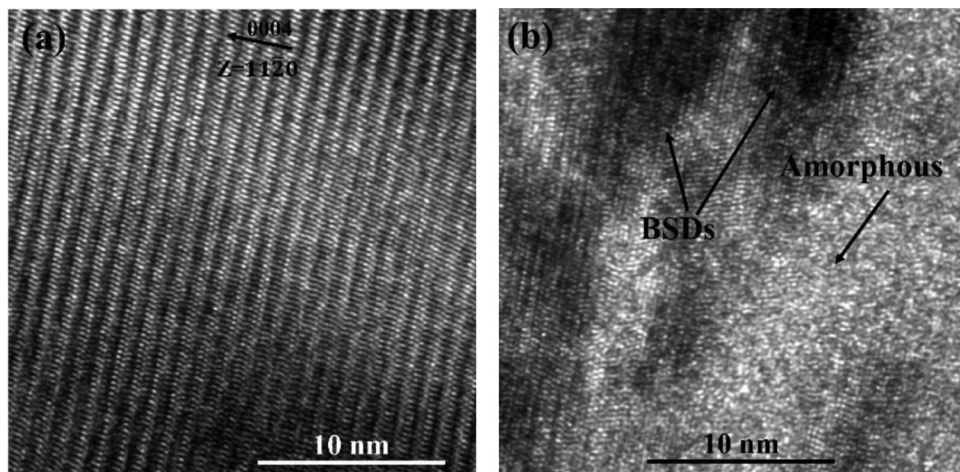
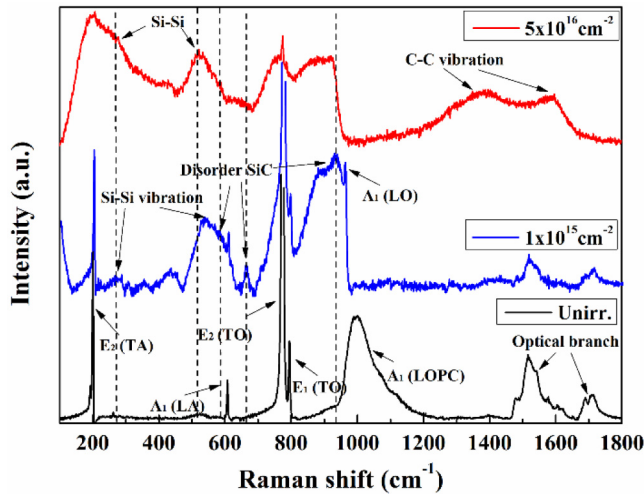


FIG. 4. High-resolution TEM images of different regions in the sample with a fluence of  $5 \times 10^{16}$  cm<sup>-2</sup>. (a) A-layer region. (b) Interface between B<sub>1</sub>- and C-layer regions. The images were taken near the [1120] zone axis.



**FIG. 5.** Raman spectra of the  $\text{He}^+$  ion-irradiated 4H-SiC irradiated at varying fluences. The spectrum for the  $5 \times 10^{16} \text{ cm}^{-2}$  fluence is taken from Ref. 6.

with our results. However, their study did not report the microstructure or defect state under that damage condition. It seems, therefore, that a region exhibiting BSDs will result in a volume swelling of 3%–7% in 4H-SiC at room temperature.

For the  $B_2$ -layer in the sample with a fluence of  $5 \times 10^{16} \text{ cm}^{-2}$ , the average BSD size is about 4.3 nm, which is smaller than that of the  $B_1$ -layer (i.e., 6.4 nm) in this sample. However, the estimated swelling value in the center part of the  $B_2$ -layer is 6.7%, which is higher than the value of 4.9% for the  $B_1$ -layer [Fig. 3(a)]. Some differences in the microstructures of these two layers cause the  $B_2$ -layer region to reach a greater swelling value. Using TEM, helium bubbles are observed only in the bottom amorphous region and the  $B_2$ -layer [Fig. 6(a)], which is consistent with the simulated  $\text{He}^+$  ion distribution profile in Fig. 1(a). Therefore, the formation of helium bubbles increases the volume swelling of this BSD-containing region.

In addition, the bottom damaged region (i.e., the  $B_2$ -level) in the sample with the highest fluence of  $1 \times 10^{17} \text{ cm}^{-2}$  exhibited a swelling value of about 3.0% [Fig. 3(b)], which is less than that of other BSD-containing regions discussed above. In the dark-field TEM image, the  $B_2$ -layer is very narrow ( $\sim 20 \text{ nm}$  wide), and only a few small BSDs are formed in this region [Fig. 1(d)]. The defect condition of the  $B_2$ -layer is similar to the A-layer of this sample, which corresponds well with their similar swelling value. The swelling of the  $B_2$ -layer in this sample confirms the transition swelling value for the point defect layer and the BSD layer.

### C. Swelling via amorphous transition

The transition to an amorphous state results in a volume swelling of about 13.3% in the sample irradiated with a fluence of  $5 \times 10^{16} \text{ cm}^{-2}$ , which is similar to the volume swelling of 12.6% for  $\text{Ni}^{3+}$  ion-irradiated 3C-SiC reported previously.<sup>10</sup> Some studies have also reported a scattered value of swelling ranging from 8% to 15% for the amorphous transition in SiC.<sup>11,23</sup> However, it should be noted that the helium bubbles formed in the amorphous region may also contribute to the swelling, and it is not clear whether this swelling value results only from the amorphous transition or it contains a contribution from helium bubbles. However, at the top part of the amorphous region in the sample irradiated with a fluence of  $1 \times 10^{17} \text{ cm}^{-2}$ , where there are no visible helium bubbles, the volume swelling is about 12.9% [Fig. 3(b)]. This is almost the same as the swelling value of the amorphous transition discussed above, confirming that the amorphous transition would result in a volume swelling of about 13% in 4H-SiC at room temperature. The swelling of the bottom amorphous layer increases to 15.3% owing to the added formation of helium bubbles [Fig. 6(b)]. Therefore, helium bubbles enlarge the volume swelling, even for amorphous SiC.

### D. Relaxation of volume swelling at the maximum damage region

Unlike the two samples irradiated with higher fluences, the volume swelling at the maximum damage region (i.e., the C-layer) of the sample irradiated with the lowest fluence is less than that of

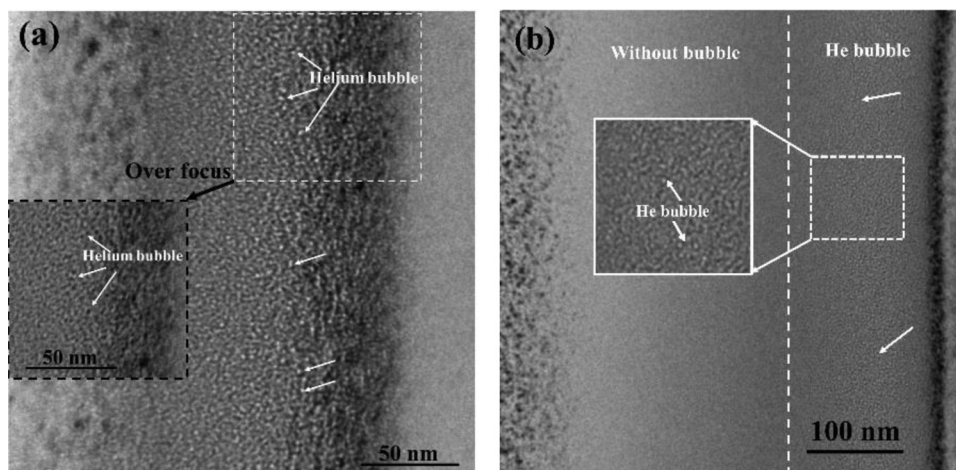


**FIG. 6.** Distribution of He bubbles in the  $\text{He}^+$  ion-irradiated 4H-SiC irradiated with fluences of (a)  $5 \times 10^{16}$  and (b)  $1 \times 10^{17} \text{ cm}^{-2}$ .

the A- and B<sub>1</sub>-layers in this sample. The swelling decreases to about 0.9% at this region, while the dose increases to 0.08 dpa [Fig. 3(c)]. The high contrast of this region in the two-beam bright-field TEM image [Fig. 1(e)] suggests a different microstructure existing in this region. It is generally considered that irradiation-induced vacancies and carbon anti-site defects (C<sub>Si</sub>), wherein C atoms occupy Si-vacancy sites, will shrink the crystal lattice.<sup>1,24</sup> Under ion irradiation, interstitials and vacancies are simultaneously introduced. Some studies have reported that only interstitials, and even restricted further to only carbon interstitials, are assumed to be mobile at temperatures below 100 °C.<sup>8,10,24</sup> Barradas *et al.* even found that excess carbon atoms were expelled from both sides of the buried oxide layer in oxygen ion-irradiated SiC at 600 °C.<sup>25</sup> However, considering the mobility of Si and C interstitials in SiC, long-range diffusion of Si or C atoms at room temperature is difficult.<sup>26</sup> Therefore, the redistribution of excess Si or C interstitials should not be the dominant reason for the decreased volume swelling at the region of the maximum damage.

For the anti-site defects, the Raman spectra observed both the Si-Si and C-C vibrations in the sample irradiated with a fluence of  $5 \times 10^{16} \text{ cm}^{-2}$  (Fig. 5), indicating the presence of Si and C anti-site defects and interstitials in the SiC. For the sample with a fluence of  $1 \times 10^{15} \text{ cm}^{-2}$ , a weak Si-Si vibration was observed; however, C<sub>Si</sub> defects, indicated by the presence of C-C vibrations, were not detected by Raman spectroscopy. This lack of C<sub>Si</sub> defects might originate from the greater ability of C to recover than that of Si, owing to the relatively higher mobility of C.<sup>10,27,28</sup> Hence, the contribution of C<sub>Si</sub> also may not be the dominant reason for the decreased volume swelling at the region of the maximum damage.

The decreased volume swelling at the maximum damage region in this sample may be associated with the ionization-induced annealing of He<sup>+</sup> ion irradiation. Zhang *et al.* have found the ionization-induced annealing of pre-existing defects in 4H-SiC at room temperature under relative high-energy (MeV) C<sup>+</sup>, O<sup>+</sup>, Si<sup>+</sup>, or Ni<sup>+</sup> ion irradiation.<sup>29</sup> In addition, they also reported a strain relaxation effect of the ionization-induced annealing.<sup>5</sup> Considering the increasing effect of the helium bubble upon the swelling in the two samples with higher He<sup>+</sup> ion fluences, it was found that the He<sup>+</sup> ion irradiation might also be used to decrease the volume swelling of SiC at room temperature. However, the mechanism for the reduction effect of He<sup>+</sup> ion irradiation on volume swelling still requires further investigation.

## V. CONCLUSION

Using TEM techniques, the defect distribution was observed and analyzed as a function of depth in selected-area He<sup>+</sup> ion-irradiated 4H-SiC irradiated at various irradiation fluences. The correlation of the swelling with various defects, including point defects or tiny clusters, BSDs, amorphous transitions, and helium bubbles, in the 4H-SiC at room temperature was separately analyzed using STEM-EELS, which provides the volume swelling range for different defect regions. A saturation of the volume swelling in the near-surface region, where only point defects and tiny clusters were introduced, was observed over fluences of  $1 \times 10^{15}$ – $1 \times 10^{17} \text{ cm}^{-2}$  at room temperature. This saturation of swelling has already reached with a value of about 2%–3% at a great low dose of

about 0.02 dpa. The swelling of the region containing BSDs ranges from about 3% to 7% at room temperature. Helium atoms in the form of helium bubbles increase the volume swelling at relatively high irradiation fluences. However, the decreasing effect of He<sup>+</sup> ion irradiation on volume swelling also seems to be possible below a certain irradiation fluence, which requires further investigation.

## ACKNOWLEDGMENTS

Part of this work was conducted at the joint-use facilities in Hokkaido University, supported by the “Microscopic Analysis for Nano materials science and Bio science Open Unit (MANBOU)” and the “Nanotechnology Platform” program of the Ministry of Education, Culture, Sports, Science and Technology (MEXT), Japan. Mr. Subing Yang thanks the Chinese Scholarship Council for supporting this work in Hokkaido University. We thank Sara Maccagnano-Zacher, Ph.D., from the Edanz Group ([www.edanzediting.com/ac](http://www.edanzediting.com/ac)) for editing a draft of this manuscript.

## REFERENCES

- 1S. Kondo, T. Hinoki, M. Nonaka, and K. Ozawa, *Acta Mater.* **83**, 1–9 (2015).
- 2A. Iveković, S. Novak, G. Dražić, D. Blagoeva, and S. G. Vicente, *J. Eur. Ceram. Soc.* **33**, 1577–1589 (2013).
- 3M. Li, X. Zhou, H. Yang, S. Du, and Q. Huang, *Scr. Mater.* **143**, 149–153 (2018).
- 4S. Castelletto, B. C. Johnson, V. Ivády, N. Stavrias, T. Umeda, A. Gali, and T. Ohshima, *Nat. Mater.* **13**, 151–156 (2014).
- 5F. X. Zhang, Y. Tong, H. Xue, J. K. Keum, Y. Zhang, A. Boule, A. Debelle, and W. J. Weber, *Appl. Phys. Lett.* **114**, 221904 (2019).
- 6S. Yang, S. Tokunaga, M. Kondo, Y. Nakagawa, and T. Shibayama, *Appl. Surf. Sci.* **500**, 144051 (2020).
- 7Y. Katoh, S. Kondo, and L. L. Snead, *J. Nucl. Mater.* **382**, 170–175 (2008).
- 8L. L. Snead, Y. Katoh, T. Koyanagi, K. Terrani, and E. D. Specht, *J. Nucl. Mater.* **471**, 92–96 (2016).
- 9T. Sawabe, M. Akiyoshi, K. Ichikawa, K. Yoshida, and T. Yano, *J. Nucl. Mater.* **386–388**, 333–337 (2009).
- 10Y. Katoh, H. Kishimoto, and A. Kohyama, *J. Nucl. Mater.* **307–311**, 1221–1226 (2002).
- 11S. Leclerc, A. Declémy, M. F. Beaufort, C. Tromas, and J. F. Barbot, *J. Appl. Phys.* **98**, 113506 (2005).
- 12Y. Katoh, L. L. Snead, I. Szlufarska, and W. J. Weber, *Curr. Opin. Solid State Mater. Sci.* **16**, 143–152 (2012).
- 13S. Leclerc, M. F. Beaufort, A. Declémy, and J. F. Barbot, *Appl. Phys. Lett.* **93**, 122101 (2008).
- 14I.-T. Bae, W. J. Weber, and Y. Zhang, *J. Appl. Phys.* **106**, 123525 (2009).
- 15A. Heft, E. Wendler, T. Bachmann, E. Glaser, and W. Wesch, *Mater. Sci. Eng. B* **29**, 142 (1995).
- 16W. J. Weber and L. M. Wang, *Nucl. Instrum. Methods Phys. Res. Sect. B* **106**, 298 (1995).
- 17D. B. Williams and C. B. Carter, *Transmission Electron Microscopy* (Plenum, New York, 1996), p. 657.
- 18R. Devanathan and W. J. Weber, *J. Nucl. Mater.* **278**, 258–265 (2000).
- 19W. Jiang, C. M. Wang, W. J. Weber, M. H. Engelhard, and L. V. Saraf, *J. Appl. Phys.* **95**, 4687–4690 (2004).
- 20C. Liu, L. He, Y. Zhai, B. Tyburska-Püschel, P. M. Voyles, K. Sridharan, D. Morgan, and I. Szlufarska, *Acta Mater.* **125**, 377–389 (2017).
- 21M. Ishimaru, R. M. Dickerson, and K. E. Sickafus, *Appl. Phys. Lett.* **75**, 352–354 (1999).

<sup>22</sup>T. Taguchi, S. Yamamoto, and H. Ohba, *Acta Mater.* **154**, 90–99 (2018).

<sup>23</sup>M. Ishimaru, I.-T. Bae, A. Hirata, Y. Hirotsu, J. A. Valdez, and K. E. Sickafus, *Phys. Rev. B* **72**, 024116 (2005).

<sup>24</sup>W. Jiang, P. Nachimuthu, W. J. Weber, and L. Ginzburgsky, *Appl. Phys. Lett.* **91**, 091918 (2007).

<sup>25</sup>N. P. Barradas, C. Jeynes, and S. M. Jackson, *Nucl. Instrum. Methods Phys. Res. Sect. B* **136–138**, 1168–1171 (1998).

<sup>26</sup>X. Yang, Y. Lu, S. Hussain, T. Duan, and P. Zhang, *J. Nucl. Mater.* **499**, 168–174 (2018).

<sup>27</sup>F. Gao and W. J. Weber, *J. Appl. Phys.* **94**, 4348 (2003).

<sup>28</sup>E. Oliviero, M. F. Beaufort, J. F. Barbot, A. van Veen, and A. V. Fedorov, *J. Appl. Phys.* **93**, 231 (2003).

<sup>29</sup>Y. Zhang, R. Sachan, O. H. Pakarinen, M. F. Chisholm, P. Liu, H. Xue, and W. J. Weber, *Nat. Commun.* **6**, 8049 (2015).